Panjawat Kongsuwan
Graduate Student
e-mail: pk2261@columbia.edu

Hongliang Wang
Graduate Student
e-mail: hw2288@columbia.edu

Department of Mechanical Engineering,
Columbia University,
New York, NY 10027

Sinisa Vukelic
Assistant Professor
Department of Mechanical Engineering,
Bucknell University,
Lewisburg, PA 17837
e-mail: sinisa.vukelic@bucknell.edu

Y. Lawrence Yao
Professor
Department of Mechanical Engineering,
Manufacturing Research Laboratory,
Columbia University,
New York, NY 10027
e-mail: yly1@columbia.edu

Characterization of Morphology and Mechanical Properties of Glass Interior Irradiated by Femtosecond Laser

Femtosecond laser pulses were focused in the interior of a single fused silica piece. Proper use of optical and laser processing parameters generated structural rearrangement of the material through a thermal accumulation mechanism, which could be potentially used for the transmission welding process. The morphology of generated features was studied using differential interference contrast optical microscopy. In addition, the predictive capability of the morphology is developed via a finite element analysis. The change in mechanical properties was studied through employment of spatially resolved nanoindentation. The specimen was sectioned and nanoindents were applied at the cross section to examine mechanical responses of the laser-modified region. Fracture toughness measurements are carried out to investigate the effects of the laser treatment on strength of the glass. [DOI: 10.1115/1.4002062]

1 Introduction

Glasses are widely used in optical, electronic, and biomedical applications because of their excellent mechanical, thermal, and optical properties. For applications such as microfluidics, lab-on-a-chip, and flat panel displays, there is a need to join glasses. Glass joining techniques based on adhesive agents are unreliable and have poor mechanical, thermal, and chemical durability [1]. Furthermore, anodic bonding, another glass joining technique, requires heating of the entire device by applying a large electrical field for an extended period of time [2]. This is undesirable as the entire device is subject to thermally induced changes due to elevated temperatures. Therefore, localized melting and joining only at the interface by transmission welding using a femtosecond pulse laser has the potential to improve reliability and durability.

Over the last decade, several research groups have studied the use of femtosecond lasers to process transparent materials. Davis et al. [3] and Glezer et al. [4] reported on the femtosecond laser induced changes in the interior of transparent materials, and discussed the potential for fabrication of photonic devices for telecommunication applications and three-dimensional optical data storages. These early reports prompted further investigation into the laser-matter interactions and the mechanisms for feature formation in transparent materials. Due to the physics of laser-matter interactions, femtosecond lasers are specifically suitable for processing dielectric materials. When a femtosecond laser pulse is focused into the interior of the material, the laser intensity around the focal volume is extremely high and causes nonlinear absorption. Consequently, permanent structural modification occurs locally at the location of the laser focus. A study of the morphology of these structural changes showed that laser energy governs the size and the numerical aperture (NA) of the objective lens governs the shape of the affected region [5]. It was also shown that the features can be induced through mechanisms dominated by localized melting or explosive plasma expansion, depending on the laser and focusing parameters [6,7].

More recently, there has been interest in joining transparent materials by utilizing the thermal accumulation mechanism. Tamaki et al. [8] first reported welding between two pieces of silica glass by femtosecond laser pulses without the insertion of an intermediate layer. The mechanical properties of the weld and treated bulk samples were then characterized by various methods. Tamaki et al. [9] conducted tensile tests to determine the joint strength; however, the testing procedure was not precise because of inability to continuously increase the applied load. Another early attempt to characterize mechanical properties of femtosecond laser-irradiated glass was done by Miyamoto et al. [10]. They performed three-point bending test and showed that the mechanical strength of the laser-melt zone was higher than that of base material; however, the sample had to be polished to unveil the laser induced feature at the bottom surface in order to experience the maximum tensile stress. Borrelli et al. [11] used a double torsion test to measure fracture toughness and investigate the strengthening effect, and revealed that the fracture toughness is increased within the laser-treated area. Bellouard et al. [12] performed nanoindentation tests on treated regions of fused silica and showed an increase in Young modulus within the laser-irradiated zones. However, these measurements were not spatially resolved and were not constrained to within the treated regions.

Studies referenced above demonstrated the feasibility of transmission welding using femtosecond lasers. However, the understanding of the changes in mechanical properties within the affected area is limited, while the changes in optical properties were well described by Schaffer et al. [13,14]. In the study presented here, two aspects are studied, the feature morphology and its mechanical properties. In order to simplify characterizations, experiments were conducted using single-piece specimens. Diffraction interference microscopy is employed to study morphology, and spatially resolved nanoindentation is used to develop a further

Contributed by the Manufacturing Engineering Division of ASME for publication in the JOURNAL OF MANUFACTURING SCIENCE AND ENGINEERING. Manuscript received November 23, 2009; final manuscript received June 21, 2010; published online July 23, 2010. Assoc. Editor: Shaochen Chen.

understanding of the change in mechanical properties such as modulus, hardness, ductility, and fracture toughness upon femtosecond laser irradiation of bulk transparent materials. The effects of laser processing parameters such as pulse energy and scanning speed on those mechanical properties are also reported.

2 Background

2.1 FS Laser Interaction and Feature Formation Mechanisms in the Interior of Glasses. When femtosecond laser pulses are focused in the interior of a transparent material, the laser intensity within the focal volume becomes extremely high resulting in nonlinear absorption. Due to the high intensity ($>10^{13}$ W/cm^2), free electrons are initially produced by multiphoton ionization. These electrons serve as seeds for subsequent avalanche ionization, through which a substantial number of free electrons will be produced. The probability of multiphoton ionization per atom per second, w_{mpi}, and that of avalanche ionization per unit time w_{avi}, are written as [15]

$$w_{mpi} \approx \omega n_{\mathrm{ph}}^{3/2}\left(\frac{\varepsilon_{osc}}{2E_I}\right)^{n_{\mathrm{ph}}} \quad \text{and} \quad w_{avi} \approx \frac{\varepsilon_{osc}}{E_I}\left(\frac{2\omega^2\nu_{\mathrm{eff}}}{\omega^2+\nu_{\mathrm{eff}}^2}\right) \tag{1}$$

where ω is the laser frequency, ν_{eff} is the electron-phonon collision frequency, n_{ph} is the number of photons necessary for the electron to be transferred from the valence to the conduction band, E_I is the ionization energy, and ε_{osc} is the electron quiver energy in the laser field. ε_{osc} has units of eV and is expressed in a scaling form [15], $\varepsilon_{osc}=9.3(1+\alpha^2)I\lambda^2/10^{14}$, where α is the coefficient for beam polarization, I is the laser intensity in units of W/cm^2, and λ is the laser wavelength in units of μm. The density of free electrons, n_e, from the two major mechanisms, multiphoton and avalanche ionization, is [15]

$$n_e(I,\lambda,t) = \left(n_0 + \frac{n_a w_{mpi}}{w_{avi}}[1-e^{-w_{avi}t}]\right) \times e^{w_{avi}t} \tag{2}$$

where n_0 is the density of initial seed electrons, n_a is the density of neutral atoms, and t is time. When the free electron density reaches the critical value, n_{cr}, the ionization threshold is achieved, and plasma is created in the material. This critical free electron density is described as [16]

$$n_{cr} = \frac{\pi m_e c^2}{e^2\lambda^2} = \frac{m_e\omega^2}{4\pi e^2} \tag{3}$$

where m_e is the electron mass, c is the speed of light, e is the electron charge, and λ is the laser wavelength. The free electron density is saturated in a few femtoseconds at the beginning of the laser pulse. During the remaining part of the pulse, plasma strongly absorbs the laser pulse energy, which creates a region of high energy density. Subsequently after the end of laser pulse, the transfer of the energy from the hot plasma to the lattice results in structural changes in the bulk transparent material [16].

Depending on the optical and laser processing parameters, the bulk transparent material can be modified through the microexplosions or thermal accumulation mechanisms [17]. For the micro-explosion mechanism when a single laser pulse is deposited into the target material, high laser intensity created by either tight focusing of low energy pulse or loose focusing of high energy pulse cause shock wave generation. The shock wave carries matter and energy away from the focal volume, compressing the surrounding material while a rarefaction wave behind the shock front propagates into the opposite direction, creating a rarified central region or void [18]. As a result, a void surrounded by densified shell is generated. The thermal accumulation mechanism occurs, when multiple pulses either with low energy and high repetition rate or with high energy and low repetition rate are irradiated at same location or at low scanning speed. Heat accumulates inside the focal volume causing the localized melting, which is followed by heat conduction into the surrounding material. Due to rapid resolidification, the melted region subsequently solidifies into a higher density phase [13]. In the latter mechanism, the feature size is determined by a combination of pulse energy and repetition rate, the stage translation speed, and the NA of the objective lens.

2.2 Characterization of Mechanical Properties by Nanoindentation. Nanoindentation or depth-sensing indentation testing is a modern technique, which can be used to characterize the mechanical properties of materials at small length scales. An analysis of a load-displacement curve gives hardness and the elastic modulus of the indented material, which are expressed as [19]

$$H_{IT}=\frac{P}{A}=\frac{P}{\pi z_p{}^2\tan^2\alpha} \quad \text{and} \quad E_{IT}=\frac{1}{2}\frac{\sqrt{\pi}}{\sqrt{A}}\frac{dP}{dz} \tag{4}$$

where H_{IT} is the indentation hardness, E_{IT} is the indentation modulus representing the combined modulus of the indenter tip and the specimen, P is the indenter maximum load, z_p is the penetration depth, dP/dz is the slope of the elastic unloading curve, and α is the semi-angle for an equivalent conical indenter.

Lawn et al. [20] studied the deformation properties of materials using indentation tests. Their primary interest is in the brittle materials especially glasses. Using the condition for compatibility of the two half-cycles at the maximum load, the elastic recovery is

$$\left(\frac{z_r}{z_m}\right)^2 = 1-\eta\frac{H}{E} \tag{5}$$

where z_r is the residual impression depth, z_m is the maximum depth of penetration, and η is the numerical constant related to Poisson's ratio and indenter's geometrical factor. From Eq. (5) the extent of recovery depends on the H/E ratio. Thus, the ratio of H/E plays an important role in identifying the elastic/plastic behavior of materials.

When dealing with an elastic/plastic field in large scale events, where cracking occurs, H/E can be related to toughness. Lawn et al. [21] showed that the quantity E/H emerges as the primary manifestation of the elastic/plastic far-field driving force for fracture. The crack opening force, P_r, produced by the residual stress field, can be expressed as $P_r \sim (E/H)^{1/2}\cot\alpha^{2/3}P$, where P is the peak indentation load, and α is the semi-angle for an equivalent conical indenter. Assuming half-penny crack geometry, the stress intensity factor due to residual far-field force is written as $K \sim f(\phi)P_r/c^{3/2}$ [22], where $f(\phi)$ is an angular function introduced to allow for the effects of the free surface, and c is the crack length. Assuming that the crack arrests when it grows to a length at which the stress intensity factor is just equal to the fracture toughness [23]. An appropriate expression of fracture toughness, K_C, evaluated by indentation testing can be written as

$$K_C = k\left(\frac{E}{H}\right)^{1/2}\frac{P}{c^{3/2}} \tag{6}$$

where k is an empirical constant that depends on the geometry of the indenter.

Because brittleness measures the relative susceptibility of a material to two competing mechanical responses, deformation and fracture, H/K_C has been proposed as the quantification of the brittleness [24] based on the critical flaw condition, $C^* = \mu_0(K_C/H)^2$, where μ_0 is the geometrical constant. The inversion of brittleness is the ductility; therefore, K_C/H, which is related to the allowable critical flaw size, represents the ductility index of materials in indentation testing.

In addition to the fracture mechanics analysis, an energy-based analysis is another approach that is used to determine elastic recovery, densification energy [25], and ductility [26] from load versus displacement curves obtained through indentation testing. Ductility is typically defined as the degree of plastic strain at fracture. The ductility index, D, is defined in terms of the indentation energy ratio as follows [26]:

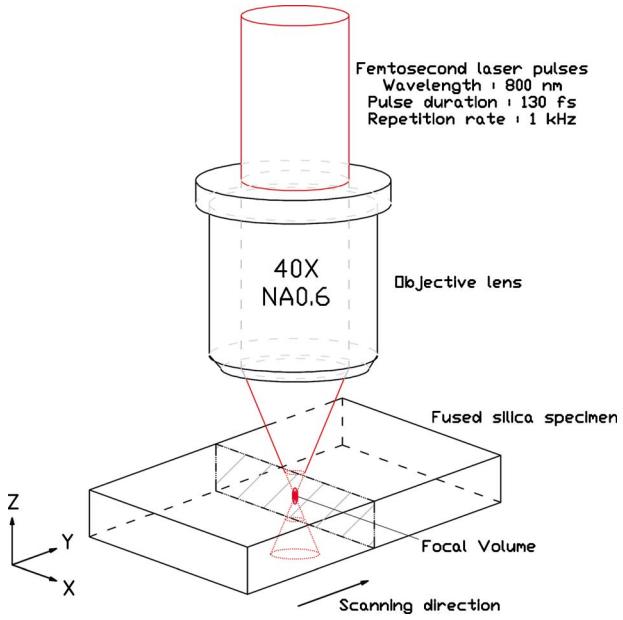

Fig. 1 Schematic illustration of experimental setup. The laser beam is focused into the interior of the fused silica sample, and the scanning direction is along the *y*-axis.

$$D = \frac{U_r}{U_t} = \frac{U_t - U_e}{U_t} = 1 - \left(\int_{z_r}^{z_m} P_{ld} dz / \int_{0}^{z_m} P_{ud} dz \right) \tag{7}$$

where U_r is the irreversible hysteresis energy, U_t is the total applied energy, U_e is the elastically recovered energy, z_r is the residual indentation depth, z_m is the maximum indentation depth, P_{ld} is the indentation load during loading, and P_{ud} is the indentation load during unloading.

3 Experimental Setup and Characterization

Experiments have been conducted utilizing a chirped amplified Ti:sapphire laser system, which outputs high energy ultrashort pulses with 800 nm wavelength and 130 fs pulse duration at a 1 kHz repetition rate. S1-UV grade fused silica was used as the base material for these experiments. The laser beam was focused by 40× objective lens with *NA* 0.60 into the interior of 1.0 mm thick, 10 mm^2 fused silica specimen mounted on a motorized linear stage. A schematic diagram of the experimental setup is illustrated in Fig. 1. Different conditions of laser processing parameters were applied by varying the feed rate of the stage and the energy of the laser pulses. Pulses were applied at energies ranging from 12 μJ to 30 μJ at stage velocities between 0.04 mm/s and 0.2 mm/s. After the femtosecond laser treatment, the samples were then sectioned, ground, and polished with cerium-oxide and a leather polishing pad. Due to the transparency of the sample, transmitted-light differential interference contrast (DIC) optical microscopy, which can reveal more contrast and detail in the feature morphology was used to obtain the side view optical micrographs.

After the femtosecond laser treatment, the affected region was examined via nanoindentation using a three-sided Berkovich indenter tip to characterize the mechanical properties. The Berkovich geometry has the advantage that the edges of the pyramid are more easily constructed to a sharper point than the four-sided Vickers geometry, and is generally used in small-scale indentation [19]. 200 nm depth spatially resolved nanoindents with 5 μm spacing in the *x* and *z* directions were conducted to cover both the affected and unaffected regions of the cross section. 2 μm deep and 440 mN load nanoindents were also performed on the features to induce cracks, which were then scanned by atomic force microscopy (AFM) to measure the crack length and investigate the change in fracture toughness of the laser-irradiated zones. Five feed rate conditions at the same energy level, 30 μJ, and another five laser pulse energy conditions at the same feed rate, 0.04 mm/s, were used to investigate the effects of laser pulse energy and laser scanning speed on feature morphology and mechanical properties due to structural modifications.

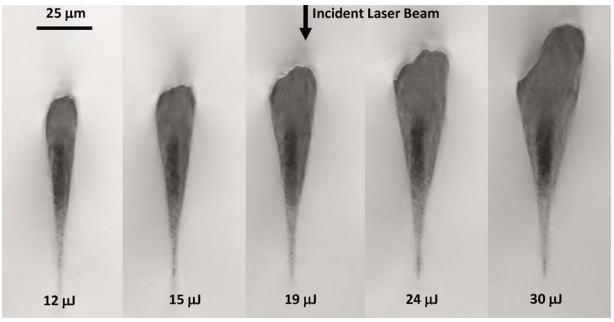

Fig. 2 Transmission DIC optical microscopy of cross section view (*x-z* plane) of femtosecond laser-irradiated fused silica (beam diameter of 1.5 μm, scanning speed of 0.04 mm/s, and rep rate of 1 kHz)

4 Results and Discussion

4.1 Experimental Morphology by Transmission DIC. As mentioned previously, when femtosecond laser pulses are focused through an objective lens to a spot inside bulk glasses, if proper conditions are met, the material confined within the focal volume experience structural modification. Usage of objectives with high *NA*s ($NA > 0.4$), feature morphologies appear to have shapes with smaller ratios of longitudinal to lateral radii [5]. This agrees well with the ratios of major to minor radii of an ellipsoidal focal volume as described by Zipfel et al. [27]. Using a three-dimensional Gaussian ellipsoid to approximate focal volume, the radii of focal volume at $1/e^2$ intensity are *NA* dependent and written as [27]:

$$\omega_{xy} = \frac{0.32\lambda}{NA}, \quad NA \leq 0.7 \quad \text{or} \quad \omega_{xy} = \frac{0.325\lambda}{NA^{0.91}}, \quad NA > 0.7$$

$$\omega_z = \frac{0.532\lambda}{[n_i - \sqrt{n_i^2 - NA^2}]} \tag{8}$$

where ω_{xy} and ω_z represent the lateral and longitudinal radii of the Gaussian ellipsoid at $1/e^2$ position in their corresponding direction, respectively, λ is the laser wavelength, and n_i is the refractive index of the transparent material.

The cross sections of features created by different laser pulse energies with a scanning speed of 0.04 mm/s and by 30 μJ laser pulses at various feed rates are seen clearly with the use of DIC optical microscopy, as shown in Figs. 2 and 3, respectively. These features have a long and narrow teardrop shape with an ellipsoidal dark core in the center. The shape and size of the core relates to the focal volume, as described by Eq. (8), and the distinctive color of this region could be a consequence of the high level of interaction of a material with laser pulses, which repeatedly deposit energy into this region with large overlap. The outer regions show some discoloration and are expected to have experienced a temperature equal or greater than the softening point of fused silica. The asymmetric shape of outer regions is considered to be the result of focusing effects [16] and different temporal slices of the energy above the threshold [1,5]. The irregular profile near the top area of the features is probably caused by the inhomogeneous distribution of the laser intensity rather than material properties. Due to the nature of the process, the focal volume can be seen as heat source. This inner darker region can be associated with focal

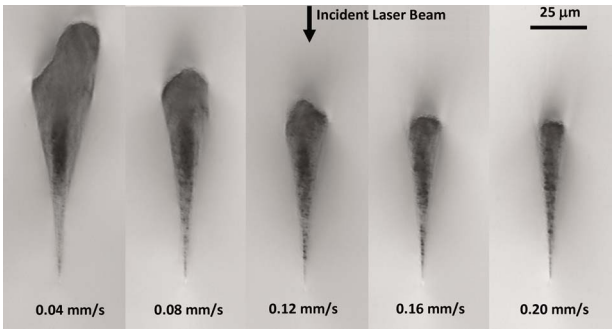

Fig. 3 Transmission DIC optical microscopy of cross section view (*x-z* plane) of femtosecond laser-irradiated fused silica (beam diameter of 1.5 μm, pulse energy of 30 μJ, and rep rate of 1 kHz)

volume, where laser energy is directly deposited and the presence of the outer region is due to heat conduction between the focal volume and surrounding material [10,13,17]. From Figs. 2 and 3, it can be seen that the feature size is strongly dependent on the scanning speed and laser pulse energy. The higher laser pulse energies and lower feed rates correspond to formation of larger features. This is particularly important for transmission welding of the glasses in flat display industry where components inside of the enclosure can be thermally sensitive and highly localized weld is desired.

Figures 4 and 5 show the feature heights, widths, and aspect ratios (height/width) as a function of laser pulse energy and laser scanning speed, respectively. The feature heights and widths are, respectively, defined from the longest and the widest portions of both regular and irregular features. For higher laser pulse energies, the temperature in the focal volume is higher, and when it is conducted to the surrounding area, the affected region, which experiences the temperature above the softening point is bigger in both directions, as shown in Fig. 4. On the other hand, the higher the speed, the less time there is for heat to accumulate inside the focal volume. As a result, the temperature is lower, and the affected region is smaller both in height and width, as shown in Fig. 5. At same laser scanning speed, 0.04 mm/s, the aspect ratios are more-or-less constant with the laser pulse energy in the range of this study, as shown in Fig. 4. This suggests that since each area of the material is processed for the same amount of time and there is no change in the focal volume ratio, the percentage of increasing in size in each direction due to different pulse energies is about the

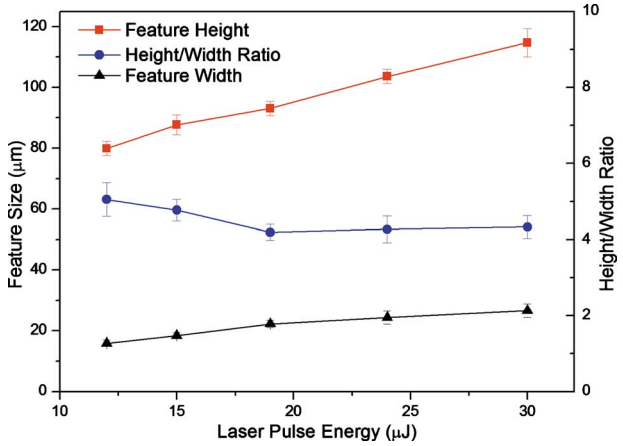

Fig. 4 Height, width, and height/width ratio of the feature (affected area as shown in Fig. 2) in femtosecond laser-irradiated fused silica at different pulse energy levels but same scanning speed of 0.04 mm/s. Error bars denote standard deviation.

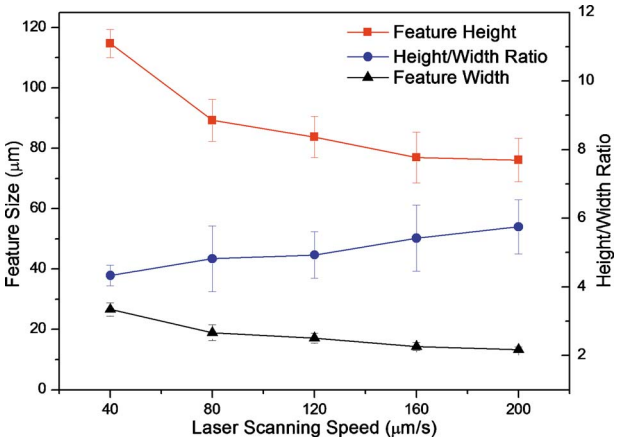

Fig. 5 Height, width, and height/width ratio of the feature (affected area as shown in Fig. 3) in femtosecond laser-irradiated fused silica at pulse energy level of 30 μJ with various scanning speeds. Error bars denote standard deviation.

same. However, from Fig. 5, the aspect ratios are decreased when the laser scanning speed is decreased, as similarly observed by Vukelic et al. [17]. Since the temperature gradients between the focal volume and the surrounding material in the axial and lateral directions are different due to the Gaussian ellipsoidal shape of the focal volume, heat flux will be greater and strongly conducts in the lateral direction. Thus, the percentage of increasing size in this direction is higher than another direction as a function of time, resulting in the decreased aspect ratios.

4.2 Morphology From Isotherm Modeling. As described in Sec. 4.1, heat accumulation and diffusion play an important role in feature formation. A simplified heat conduction model was used in order to capture the basic mechanisms of structure changes and to predict the size of the softening/melting region induced by femtosecond laser processing of transparent materials. The work piece material is assumed to be isotropic, and the temperature dependence of thermal conductivity and specific heat is taken into account. Modeling includes deposition of the femtosecond laser pulses at a 1 kHz repetition rate into the interior of a finite three-dimensional plate of fused silica. One-temperature heat conduction equation has been solved since the two-temperature model is suitable only for low fluences and widely used for metals [28]. The governing equation is therefore the temperature dependent classical heat equation with a laser source:

$$\rho C_p(T)\frac{\partial T}{\partial t} = \nabla(k(T)\,\nabla\, T) + I(x,y,z,t) \tag{9}$$

where ρ is density, Cp is specific heat, k is conductivity, x, y, and z are the Cartesian coordinates, t is time, and I is the laser intensity or the energy rate supplied externally into the body. Laser energy is assumed to be absorbed only inside a focal volume. Based on Eq. (8), the focal volume is modified to use a double ellipsoidal shape in order to compensate for a teardrop shape of features caused by focusing effects [16]. Therefore, the intensity profile of a moving laser beam is a 3D spatial Gaussian ellipsoid and a 1D Gaussian in time, which can be written as

$$I(x,y,z,t) = I_0 \exp\left[\frac{-2((\Delta x)^2+(\Delta y)^2)}{\omega_{xy}^{\,2}}\right]\exp\left[\frac{-2(\Delta z)^2}{\omega_z^{\,2}}\right] \times\exp\left[-4\ln 2\left(\frac{t-2t_p}{t_p}\right)^2\right] \tag{10}$$

where I_0 is the peak intensity, Δx, Δy, and Δz are distances measured in Cartesian coordinate system from the center of the laser beam, and t_p is a full-width-at-half-maximum (FWHM) pulse width. The aspect ratio of the focal volume, ω_z/ω_{xy}, is kept con-

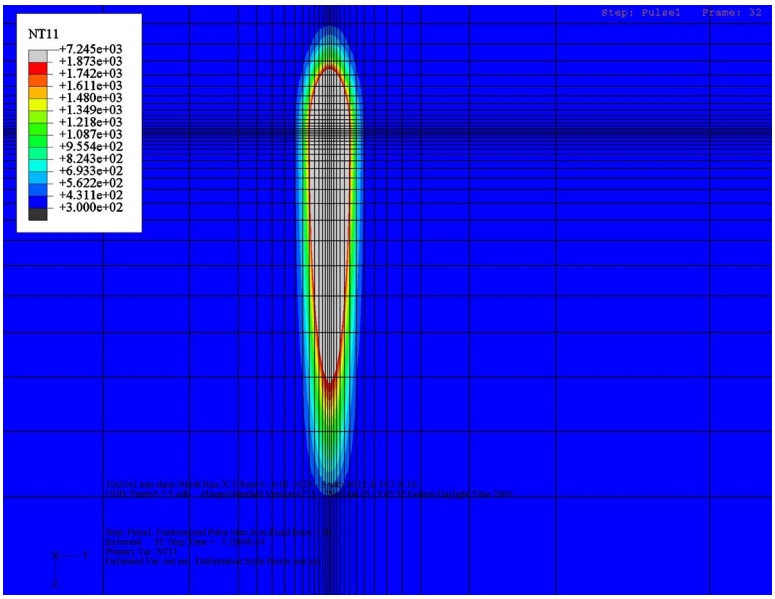

Fig. 6 Representative temperature distribution in femtosecond laser-irradiated fused silica at pulse energy level of 30 μJ and scanning speed of 0.04 mm/s. The gray area represents the material region that experiences the temperature equal or greater than the softening point (step time of 520 fs).

stant as it depends on wavelength and *NA* only, which are constant. Although simplified with respect to actual process, the established numerical model allows one to estimate the size of the affected region based on the input parameters, laser pulse energy, repetition rate and feedrate. The analysis is implemented with the commercial finite element method (FEM) program ABAQUS/STANDARD.

The representative isothermal contours of the affected region during processing using 30 μJ laser pulse energy and 0.04 mm/s laser scanning speed is illustrated in Fig. 6. The gray color contour represents the material region that experiences temperatures equal to or greater than the softening temperature of fused silica. This contour shape is similar to the feature morphology, as shown in Figs. 2 and 3. The feature sizes and aspect ratios of these numerical results along with the experimental ones are plotted as a function of laser pulse energy in Fig. 7. The numerical models predict the same increasing trend of feature size as the experimental results both in height and width, as shown in Fig. 7(*a*), and also the same more-or-less constant trend of the aspect ratios as the experimental ones, as shown in Fig. 7(*b*). However, there is some discrepancy between the numerical and experimental sizes. This is due to the fact that the numerical model does not take into account hydrodynamic motion and shock wave that comes as its consequence, as well as pressure effect. As a result, the size of the feature is underestimated. From Fig. 7(*a*), it is clearly seen that there is higher discrepancy in the prediction of the feature widths. Thus, it could be thought that the effects of shock wave and pressure are more dominant in determining the feature size in the lateral direction than in the axial direction. Subsequently, the aspect ratios are overestimated, as seen in Fig. 7(*b*). Therefore, the thermal model suggests that the mechanisms responsible for feature formation of femtosecond laser-irradiated fused silica using low repetition rate, high energy regime, and low scanning speed are more complex and could be the combinations of high pressure explosive plasma expansion and high temperature thermal diffusion. Future studies will concentrate on further improvement of the established numerical model.

4.3 Spatially Resolved Nanoindentation. An array of 200 nm depth nanoindentation measurements were performed over the cross section of femtosecond laser-modified fused silica with a spatial resolution of 5 μm, as shown by the reflection DIC optical micrograph in Fig. 8. The radius of plastic zone from a cavity model of an elastic-plastic indentation by a conical indenter, which described by Johnson [29], was used as a guideline to define the spacing between each indent. The plastically deformed radius is written as

$$r_p = \frac{d}{\tan\beta}\left[\frac{E\tan\beta}{6Y(1-\nu)} + \frac{2-4\nu}{3-3\nu}\right]^{1/3} \tag{11}$$

where r_p is the radius of plastic zone, d is the indentation depth, β is the angle between the indenter face and the surface (19.7 deg for the equivalent cone for a Berkovich indenter), E is Young's modulus, Y is the yield stress, and ν is Poisson's ratio. The load-displacement curves of indents on both modified and unmodified regions in Fig. 8 were measured, and the representative curves of these two regions were compared, as illustrated in Fig. 9. Hardness and Young's modulus are extracted from the loading and unloading curves, respectively.

The contour maps of two basic material properties, Young's modulus and hardness, correspond to the array of nanoindents in the optical micrograph were plotted, as shown in Fig. 10. It is observed that Young's modulus and hardness in the femtosecond laser-irradiated region are reduced, and that the size and shape of these contours look similar to the morphology of the affected region in Fig. 8. The reduction in modulus and hardness confirms the presence of structural modifications inside the affected region. The region undergoes irreversible densification, which is a consequence of high pressures created by the plasma expansion. At the same time, the presence of breaks in the linkage within a structure due to the nature of the process also allows easier displacement of the atoms and reduces the elastic modulus [30]. Young's modulus should be proportional to the number of bridging bonds per unit volume of glass [31], and the hardness relates to the connectivity of the structure [32]. From fluorescence microscopy it was shown that, in fused silica, nonbridging oxygen hole centers (NBOHCs) are formed in the regions exposed to femtosecond laser irradiation, especially in high pulse energy regime [14]. NBOHCs are considered as defects and cause the connectivity of glass network

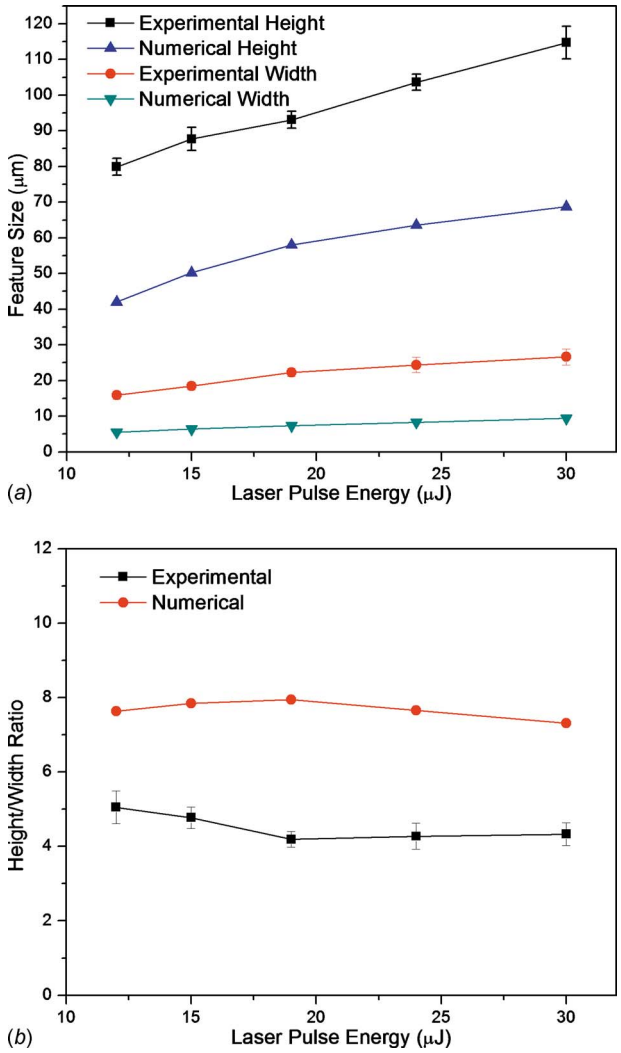

Fig. 7 Experimental and numerical feature morphology comparison: (*a*) feature size (*b*) height/width ratio of femtosecond laser-irradiated fused silica at different pulse energy levels with the same scanning speed of 0.04 mm/s. Error bars denote standard deviation.

structure to be decreased. Therefore, the combination of high pressure and high temperature generated by femtosecond laser pulse trains cause the material in the affected region to become more flexible (lower E) and softer (lower H). As the point that has the lowest value of Young's modulus and hardness shown in Fig. 10 is aligned with the optical axis of laser pulses and is almost in the middle of the feature, it could be the center of the intensive interaction region as discussed in Sec. 4.1, and the existence of this weakest point is a consequence of that.

Figure 11 shows the spatially resolved mapping of H/E ratios over the femtosecond laser-irradiated region. It is observed that the H/E ratios in the femtosecond laser-irradiated region are reduced. When focusing on elastic and plastic strains and considering each of the two properties, Young's modulus and hardness, materials with lower values of Young's modulus exhibit lower resistance to elastic deformation or higher elastic strain, while materials with lower values of hardness exhibit lower resistance to plastic deformation or higher plastic strain. However, in displacement-controlled nanoindentation, there is the same amount of total strain, and the elastic and plastic strain portions cannot increase or decrease at the same time. Thus, the changes of these two properties will compete with each other, and the materials will show their changes in elastic/plastic behavior. Plastic

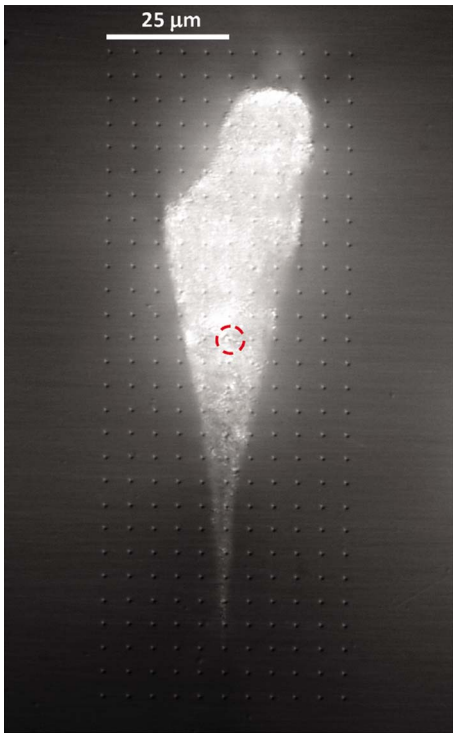

Fig. 8 Representative reflection DIC optical microscopy of spatially resolved nanoindentation array (200 nm depth and 5 μm spacing) on the cross section (*x-z* plane) of fused silica irradiated by femtosecond laser. The circle locates the weakest point in Young's modulus and hardness corresponds to Fig. 10.

behavior dominates at lower values of H/E, while elastic behavior dominates at higher values of H/E. Therefore, the decrease in H/E ratios means the material in the modified region experiences a higher degree of plastic deformation, which can be viewed as an increase in ductility.

Furthermore, one can determine the ductility index through employment of Eq. (7). The ratio of the irreversible hysteresis loop energy U_r to the total energy, U_t, is defined as the degree of plastic flow [26]. The ductility index D varies from 0.0 for a purely elastic to 1.0 for a purely plastic material. A mapping of the results from this approach is illustrated in Fig. 12. The contour map

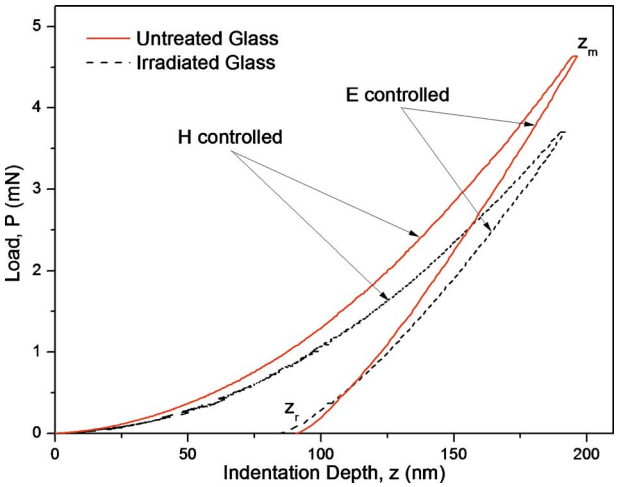

Fig. 9 Representative load-displacement curves for 200 nm indentation in untreated and irradiated regions of fused silica sample

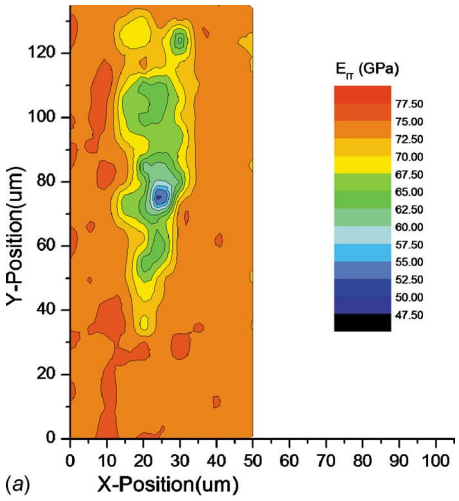

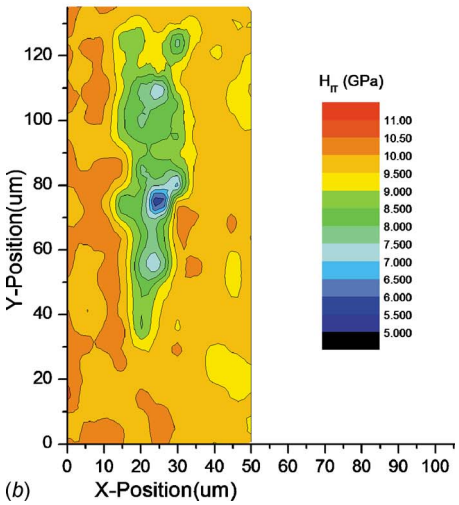

Fig. 10 Spatially resolved determination of (*a*) Young's modulus (*b*) hardness on the cross section of laser-irradiated region (30 μJ pulse energy and 0.04 mm/s scanning speed). The maps correspond to the array of 200 nm depth nanoindents with 5 μm spacing shown in Fig. 8 and are constructed based on the load-displacement measurement results shown in Fig. 9.

showed that the ductility index of femtosecond laser-irradiated region is increased up to 25%. The increase in ductility index corresponds well with the highly plastic behavior indicated by the decrease in H/E ratio.

With the "open" network structure of fused silica, it is considered that the main mechanism for plastic deformation is densification rather than plastic flow [33] and that the irreversible hysteresis loop energy U_r can also be defined as the energy consumed for densification [25]. The increase in normalized irreversible loop energy shown in Fig. 12 corresponds to the increase in refractive index of the treated glass [13]. Spatially resolved and decomposed Raman spectral analysis [17] revealed that the volume fraction of three- and fourfold rings of affected regions irradiated by 30 μJ pulse energy and 0.04 mm/s scanning speed increases as illustrated in the contour map of Fig. 13. The densification has been related to the change of structure from five- and sixfold rings to become three- and fourfold rings, which have smaller intertetrahedral angles and thus are more densely packed. Therefore, in addition to the increase in refractive index [13,14], as well as the structural changes characterized by spatially resolved Raman spectroscopy [17], the increase in normalized dissipated energy by spatially resolved nanoindentation testing also suggested that

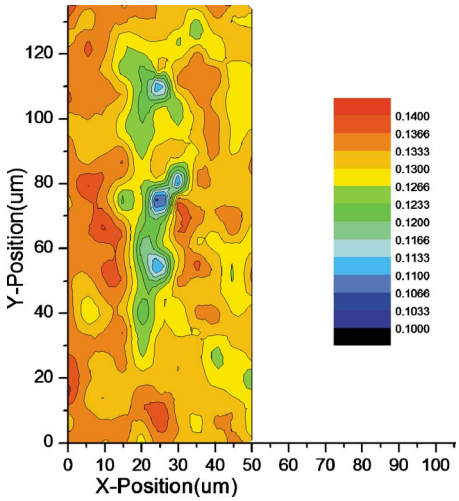

Fig. 11 Spatially resolved determination of the ratio between hardness and Young's modulus (H/E) on the cross section of laser-irradiated region (30 μJ pulse energy and 0.04 mm/s scanning speed). The maps correspond to the array of 200 nm depth nanoindents with 5 μm spacing shown in Fig. 8 and are constructed based on the load-displacement measurement results shown in Fig. 9.

fused silica irradiated by femtosecond laser pulses undergoes densification.

Toughness, a measure of the ability of a material to absorb energy up to fracture, is an integration product of strength and degree of plastic strain or ductility. Considering the conservation of the volume in the cavity model, Johnson [29] located the elastic-plastic boundary for conical or pyramidal indenters during contact. The expression, which relates hardness, H, to yield strength, Y, and Young's modulus, E, is written as

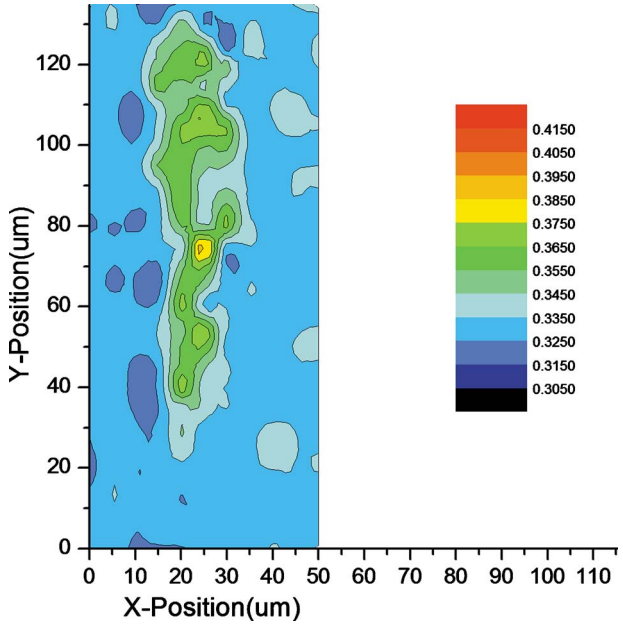

Fig. 12 Spatially resolved determination of the normalized dissipated energy on the cross section of laser-irradiated region (30 μJ pulse energy and 0.04 mm/s scanning speed). The maps correspond to the array of 200 nm depth nanoindents with 5 μm spacing shown in Fig. 8 and are constructed based on the load-displacement measurement results shown in Fig. 9. The maps represent ductility index and densification.

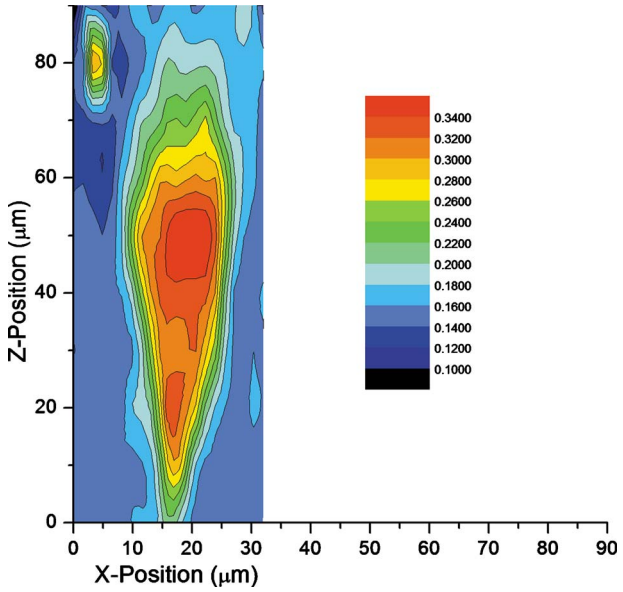

Fig. 13 Volume fraction distribution of three- and fourfold ring structures based on the 606 cm^{-1} and 495 cm^{-1} peaks in Raman spectra of cross section of femtosecond laser-irradiated region (30 μJ pulse energy and 0.04 mm/s scanning speed) [17]

$$\frac{H}{Y} = \frac{2}{3}\left[1 + \ln\left(\frac{E\tan\beta}{6(1-\nu)Y} + \frac{2(1-2\nu)}{3(1-\nu)}\right)\right] \tag{12}$$

where β is the angle between the indenter face and the surface, and ν is Poisson's ratio. As can be seen from this equation, when H/E is decreased, the yield strength is also decreased. Femtosecond laser-irradiated regions showed a decrease in yield strength and an increase in ductility. Thus, the changes in toughness result from the competitions between the percentage decrease in yield strength and the percentage increase in ductility. If the change in yield strength was less dominant, the affected regions of fused silica would have higher toughness.

4.4 Effect of Laser Processing Parameters on Mechanical Responses. As demonstrated previously, the materials in the affected region are more flexible (lower E), softer (lower H), and highly plastic (lower H/E ratio). Referring to the difference of each property between the untreated and the irradiated regions, Figs. 14 and 15 show the maximum decrease of modulus, E, hardness to modulus ratio, H/E, and hardness, H, as a function of laser pulse energy and laser scanning speed, respectively. All three quantities show decreasing trends in cases of increasing pulse energy or decreasing scanning speed. The decreasing trend of the H/E ratios revealed more dominant plastic behavior in the new structural materials created by more energetic pulses or by slower scanning speeds. Due to higher pressures and temperatures caused by more energetic pulses, the mean separation between the atoms increases, and the structure of the irradiated glass tends to exhibit more breaks in the linkage. Thus, the more NBOHCs are created, and the connectivity of the structure decreases. Therefore, E and H decrease further with an increase in laser pulse energy. On the other hand, the lower the speed, the more interaction time and a higher number of pulses are used to modify the network structure of the glass. As a result, there are more NBOHCs, and the connectivity of the structure decreases. Therefore, there is a further decrease in E and H due to the decrease in laser scanning speed.

4.5 Fracture Toughness Comparison. Cracks were produced in the glass using 2 μm depth displacement-controlled and 440 mN load-controlled nanoindentation tests. Due to the feature size and the residual imprint size, only one or two indents could be placed on each feature as shown by the reflection DIC optical micrograph in Fig. 16. After indentation, the fused silica samples were scanned by AFM to investigate and measure the final crack lengths, c, from the center of the residual impression to the ends of cracks at specimen surface, as shown in Fig. 17. The decrease in H/E ratios of the affected regions, as shown in Sec. 4.3, which represents highly plastic behavior, will cause the larger impression lengths, a, measured from the center of the contact to the corners of the impression. As expected, the final crack lengths, c, which should have a direct relationship with the impression lengths, were larger in the affected regions that were created by both load- and displacement-controlled nanoindentations.

From the final crack length, c, max load, P, and the E/H ratio, the fracture toughness, K_{IC}, in the femtosecond laser-irradiated regions was calculated as a function of laser pulse energy and laser scanning speed and compared with the values from the untreated regions, as shown in Fig. 18. Although the higher E/H ratios of the modified materials enhance the residual forces, which drive the crack, the power of the E/H term is three times less than that of the c term in Eq. (5). Thus, the fracture toughness is de-

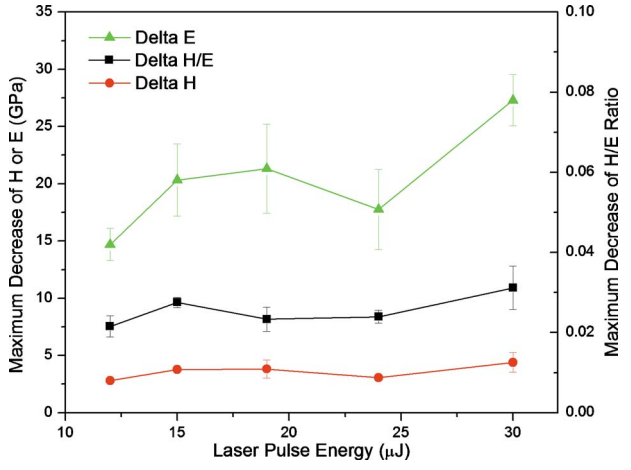

Fig. 14 Maximum decrease of modulus (E), hardness (H), and hardness to modulus ratio (H/E) of 200 nm depth nanoindents inside the femtosecond laser-irradiated regions (same scanning speed of 0.04 mm/s but different pulse energy levels.) Error bars denote standard error.

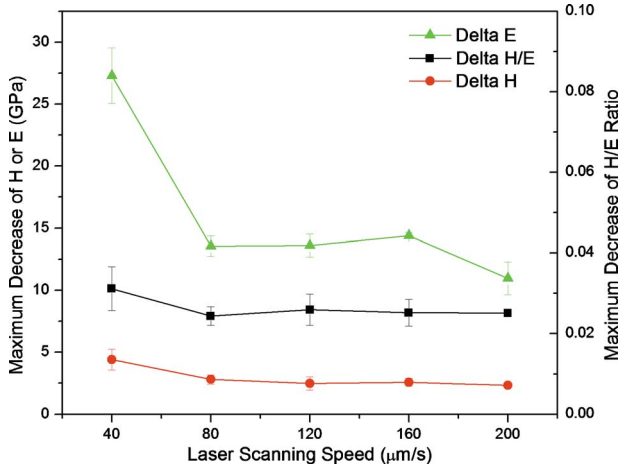

Fig. 15 Maximum decrease of modulus (E), hardness (H), and hardness to Young's modulus ratio (H/E) of 200 nm depth nanoindents inside the femtosecond laser-irradiated regions (same pulse energy level of 30 μJ with various scanning speeds). Error bars denote standard error.

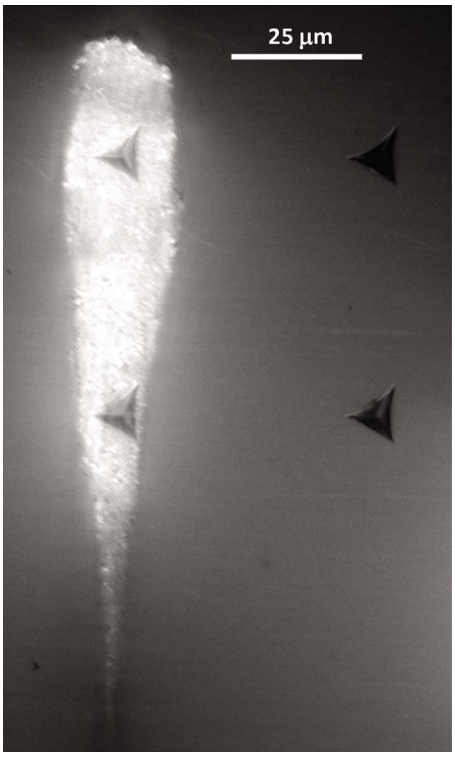

Fig. 16 Reflection DIC optical microscopy of 2 μm depth nanoindents on and off the femtosecond laser-irradiated region for fracture toughness measurements

creased compared to the untreated regions. However, the brittleness index H/K_C in the affected region is decreased as well, which corresponds to the increase in ductility index. As shown previously in Figs. 14 and 15, the H/E ratios were more reduced in cases of increased laser pulse energy and decreased laser scanning speed. The increase in E/H ratios and the larger crack lengths, c, in cases of increasing pulse energy or decreasing scanning speed, cause decreasing trends of fracture toughness, as shown in Fig. 18. It is shown that the maximum decrease is less than 10%, and the decrease in fracture toughness can be minimized if lowering the pulse energies or increasing the scanning speeds.

5 Conclusion

The interior of fused silica was irradiated by femtosecond laser pulses with pulse energies higher than the threshold for multiphoton and avalanche ionization. The morphology of the affected regions has been investigated, and it has been observed that the feature size increased in both height and width with an increase of the laser pulse energy or with decrease of the scanning speed. The aspect ratios remain more-or-less constant with pulse energy due to the constant size of focal volume and constant interaction time. Furthermore, an increase with scanning speed is due to reduced interaction time and the preferable direction of heat conduction caused by the differences in temperature gradients between the radial and longitudinal directions. Spatially resolved measurements of mechanical properties, i.e., hardness, Young's modulus, and H/E ratios, on cross sections of the affected regions were performed. Decreases in Young's modulus and hardness were observed due to higher content of the NBOHCs in treated regions that cause lower connectivity of the atomic structure caused by energetic pulse interaction with the material. However, the new structural material exhibits greater plastic behavior, and the ductility increases. This study has also shown that the fracture toughness is slightly decreased ($<10\%$) and the processing conditions of this study could be used for transmission welding applications. Furthermore, this study has shown that the decrease in fracture toughness can be minimized by lowering the laser pulse energy or increasing the laser scanning speed.

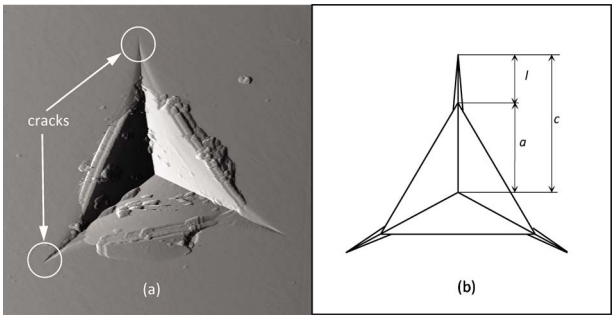

Fig. 17 (*a*) AFM scan (the derivative of topography) of 2 μm depth indentation. (*b*) Crack parameters for Berkovich indenter. Crack length *c* is measured form the center of the residual impression to the tip of crack at specimen surface.

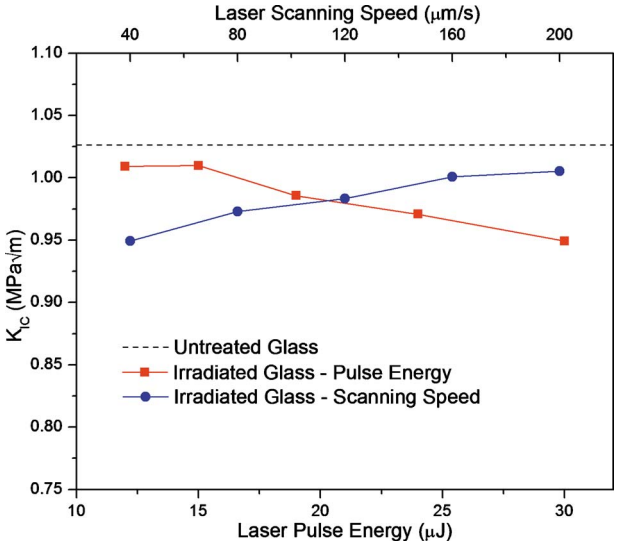

Fig. 18 Comparison of fracture toughness measured by crack-induced indentation method between untreated and irradiated regions at 30 μJ pulse energy with various scanning speeds, and at different pulse energy levels with 0.04 mm/s scanning speed of fused silica sample

References

[1] Miyamoto, I., Horn, A., Gottmann, J., Wortmann, D., and Yoshino, F., 2007, "Fusion Welding of Glass Using Femtosecond Laser Pulses With High-Repetition Rates," J. Laser Micro/Nanoeng., **2**(1), pp. 57–63.

[2] Kutchoukov, V. G., Laugere, F., van der Vlist, W., Pakula, L., Garini, Y., and Bossche, A., 2004, "Fabrication of Nanofluidic Devices Using Glass-to-Glass Anodic Bonding," Sens. Actuators, A, **114**(2–3), pp. 521–527.

[3] Davis, K. M., Miura, K., Sugimoto, N., and Hirao, K., 1996, "Writing Waveguides in Glass With a Femtosecond Laser," Opt. Lett., **21**(21), pp. 1729–1731.

[4] Glezer, E. N., Milosavljevic, M., Huang, L., Finlay, R. J., Her, T.-H., Callan, J. P., and Mazur, E., 1996, "Three-Dimensional Optical Storage Inside Transparent Materials," Opt. Lett., **21**(24), pp. 2023–2025.

[5] Schaffer, C. B., Jamison, A. O., and Mazur, E., 2004, "Morphology of Femtosecond Laser-Induced Structural Changes in Bulk Transparent Materials," Appl. Phys. Lett., **84**(9), pp. 1441–1443.

[6] Schaffer, C. B., Brodeur, A., Garcia, J. F., and Mazur, E., 2001, "Micromachining Bulk Glass by Use of Femtosecond Laser Pulses With Nanojoule Energy," Opt. Lett., **26**(2), pp. 93–95.

[7] Glezer, E. N., and Mazur, E., 1997, "Ultrafast-Laser Driven Micro-Explosions in Transparent Materials," Appl. Phys. Lett., **71**(7), pp. 882–884.

[8] Tamaki, T., Watanabe, W., Nishii, J., and Itoh, K., 2005, "Welding of Trans-

parent Materials Using Femtosecond Laser Pulses," Jpn. J. Appl. Phys., Part 2, **44**(22), pp. L687–L689.
[9] Tamaki, T., Watanabe, W., and Itoh, K., 2006, "Laser Micro-Welding of Transparent Materials by a Localized Heat Accumulation Effect Using a Femtosecond Fiber Laser at 1558 nm," Opt. Express, **14**(22), pp. 10460–10476.
[10] Miyamoto, I., Horn, A., Gottmann, J., Wortmann, D., Mingareev, I., Yoshino, F., Schmidt, M., Bechtold, P., Okamoto, Y., Uno, Y., and Herrmann, T., 2008, "Novel Fusion Welding Technology of Glass Using Ultrashort Pulse Lasers," Proceedings of the 27th International Congress on Applications on Lasers & Electro-Optics, Temecula, CA, M304, pp. 112–121.
[11] Borrelli, N., Helfinstine, J., Price, J., Schroeder, J., Streltsov, A., and Westbrook, J., 2008 "Glass Strengthening With an Ultrafast Laser," Proceedings of the 27th International Congress on Applications on Lasers & Electro-Optics, Temecula, CA, M404, pp. 185–189.
[12] Bellouard, Y., Colomb, T., Depeursinge, C., Dugan, M., Said, A. A., and Bado, P., 2006, "Nanoindentation and Birefringence Measurements on Fused Silica Specimen Exposed to Low-Energy Femtosecond Pulses," Opt. Express, **14**(18), pp. 8360–8366.
[13] Schaffer, C. B., Garcia, J. F., and Mazur, E., 2003, "Bulk Heating of Transparent Materials Using a High-Repetition-Rate Femtosecond Laser," Appl. Phys. A: Mater. Sci. Process., **76**, pp. 351–354.
[14] Krol, D. M., 2008, "Femtosecond Laser Modification of Glass," J. Non-Cryst. Solids, **354**, pp. 416–424.
[15] Gamaly, E. G., Rode, A. V., Luther-Davies, B., and Tikhonchuk, T. V., 2002, "Ablation of Solids by Femtosecond Lasers: Ablation Mechanism and Ablation Thresholds for Metals and Dielectrics," Phys. Plasmas, **9**(3), pp. 949–957.
[16] Gamaly, E. G., Juodkazis, S., Nishimura, K., Misawa, H., Luther-Davies, B., Hallo, L., Nicolai, P., and Tikhonchuk, V. T., 2006, "Laser-Matter Interaction in the Bulk of a Transparent Solid: Confined Microexplosion and Void Formation," Phys. Rev. B, **73**, p. 214101.
[17] Vukelic, S., 2009, "Laser Induced Deformation and Structural Modification of Crystalline and Amorphous Materials," Ph.D. thesis, Columbia University, New York, NY.
[18] Juodkazis, S., Masawa, H., Hashimoto, T., Gamaly, E.G., and Luther-Davies, B. 2006 "Laser-Induced Microexplosion Confined in a Bulk of Silica: Formation of Nanovoids," Appl. Phys. Lett., **88**(20), pp. 201909.
[19] Fischer-Cripps, A. C., 2004, *Nanoindentation*, Springer, New York, Chap. 2.
[20] Lawn, B. R., and Howes, V. R., 1981, "Elastic Recovery at Hardness Indentations," J. Mater. Sci., **16**, pp. 2745–2752.
[21] Lawn, B. R., Evans, A. G., and Marshall, D. B., 1980, "Elastic/Plastic Indentation Damage in Ceramics: The Median/Radial Crack System," J. Am. Ceram. Soc., **63**(9–10), pp. 574–581.
[22] Sih, G. C., 1973, *Handbook of Stress Intensity Factors*, Lehigh University Press, Bethlehem, PA.
[23] Pharr, G. M., Harding, D. S., and Oliver, W. C., 1993, "Measurement of Fracture Toughness in Thin Films and Small Volume Using Nanoindentation Methods," *Mechanical Properties and Deformation Behavior of Materials Having Ultra-Fine Microstructures*, M. Nastasi, ed., Kluwer Academic, The Netherlands, pp. 449–461.
[24] Lawn, B. R., and Marshall, D. B., 1979, "Hardness, Toughness, and Brittleness: An Indentation Analysis," J. Am. Ceram. Soc., **62**(7–8), pp. 347–350.
[25] Suzuki, K., Benino, Y., Fujiwara, T., and Komatsu, T., 2002, "Densification Energy During Nanoindentation of Silica Glass," J. Am. Ceram. Soc., **85**(12), pp. 3102–3104.
[26] Sakai, M., 1999, "The Meyer Hardness: A Measure for Plasticity?," J. Mater. Res., **14**(9), pp. 3630–3639.
[27] Zipfel, W. R., Williams, R. M., and Webb, W. W., 2003, "Nonlinear Magic: Multiphoton Microscopy in the Biosciences," Nat. Biotechnol., **21**(11), pp. 1369–1377.
[28] Jiang, L., and Tsai, H.-L., 2005, "Improved Two-Temperature Model and Its Application in Ultrashort Laser Heating of Metal Films," ASME J. Heat Transfer, **127**, pp. 1167–1173.
[29] Johnson, K. L., 1985, *Contact Mechanics*, Cambridge University Press, Cambridge, Chap. 6, pp. 171–175.
[30] Shelby, J. E., 1997, *Introduction to Glass Science and Technology*, The Royal Society of Chemistry, Cambridge, UK.
[31] Charles, R. J., 1961, "A Review of Glass Strength," *Progress in Ceramic Science*, Vol. 1, J. E. Burke, ed., Pergamon, New York, pp. 1–38.
[32] Varshneya, A. K., 1994, *Fundamentals of Inorganic Glasses*, Academic, New York.
[33] Hagan, J. T., 1979, "Cone Cracks Around Vickers Indentations in Fused Silica Glass," J. Mater. Sci., **14**, pp. 462–466.